Metrology of thin adaptive optics for X-ray beamlines

Kenneth Buffo[a,*], Casey DeRoo[a], Philip Griffin[a], Antoine Islegen-Wojdyla[b], Xiaoya Chong[b], Kenneth Goldberg[b], Bryan Ochoa[b], Susan Trolier-McKinstry[c], and Pannawit Tipsawat[c]

[a]University of Iowa, Department of Physics and Astronomy, Iowa City, Iowa, IA, USA
[b]Advanced Light Source, Lawrence Berkeley National Laboratory, Berkeley, CA, USA
[c]Penn State University, Materials Science and Engineering Department and Materials Research Institute, Millennium Science Complex, University Park, PA, USA

ABSTRACT

The generational advances in synchrotron radiation sources have historically been bottlenecked by the optics used to focus and manipulate X-ray beamlines. Such optics have strict metrology requirements while needing to be versatile in their abundance of applications. To meet these requirements, thin adaptive optics (TAOs) have been developed to correct optical surface error and perform source wavefront shaping. These TAOs consist of a series of thin-film piezoelectric actuators deposited on a mirror substrate that induce spatially localized figure deformations. In this work, the fabrication and actuator performance of two TAO mirror segments are reported. These ~ 0.5 mm thick optics have addressable actuators whose responses were measured using Fizeau interferometry. The individual actuator responses of the two TAOs induced a figure change peak-to-valley (PV) of 183 nm and 63 nm on average. Finally, the TAOs were used to measure the deflection of an optical laser under operation of their actuators. These laser deflections were shown to be repeatable under a phase-shifted measured period. The metrology characterization described in this work shows a promising future for TAO development in realizing figure correction and wavefront shaping in X-ray beamlines.

Keywords: X-ray optics, adjustable optics, metrology, synchrotron optics, thin-film piezoelectric

*Address all correspondence to: Kenny Buffo, E-mail: kbuffo@uiowa.edu

1. INTRODUCTION

The current generation of X-ray diffraction limited storage rings (XDLSRs) and free electron lasers (FELs) offer exquisite brightness and beam coherence. These synchrotrons have been used for probing materials at an unprecedented scale, from observing femtosecond-resolved molecular structural dynamics,[1] using time-resolved resonant inelastic X-ray scattering to observe spin and orbital correlations in doped insulators,[2] to achieving 16 nm isotropic resolution when performing 3D tomographic reconstructions of materials.[3] Given that these synchrotrons are able to produce beams with emittances < 100 pm·rad, this places challenging requirements on the X-ray optics used to focus them, especially given the diversity of beamline applications. As an example, the Strehl ratio is defined as the ratio of a measured beam intensity to the ideal intensity. To achieve a Strehl ratio of 0.95, the Linac Coherent Light Source required X-ray mirrors with < 0.5 nm surface height deviation.[4] The development of such exquisite mirrors has been a long-standing challenge from both a manufacturing and metrology standpoint.[5]

To address the need for exquisitely shaped X-ray mirrors, thin adaptive optics (TAOs) have been prototyped. These ~ 0.5 mm thick optics employ a set of thin-film (2.8 μm thick), lead zirconate titanate (PZT) piezoelectric actuators deposited on one side. The actuators can induce localized deformations to the optic surface, performing both static and high frequency figure changes. Static and low frequency changes are meant to correct for optical aberrations, mounting flexure, thermal drift, and swapping of beam focal length based on energy. High frequency figure changes can be used for active feedback in coherent diffraction imaging as well as beam pointing and wavefront shaping in FELs, a common application in pump-probe experiments.[6]

Adaptive optics have previously been applied to X-ray beamlines,[7] with thin-film PZT optics more widely developed on flat and curved substrates for use in astronomy.[8,9] There are some important differentiators between devices that rely on bulk piezoelectric devices and those that rely on thin films for the beam shaping. First, the

Advances in X-Ray/EUV Sources, Optics, and Components XX, edited by Ali M. Khounsary, Hidekazu Mimura, Proc. of SPIE Vol. 13620, 136200M · 2025 Published by SPIE
0277-786X · doi: 10.1117/12.3063585

operating voltages of thin films are far smaller than those of bulk piezoelectric actuators. The induced strain depends on the magnitude of the electric field which is applied; thus, the smaller distance between the electrodes of thin film devices produces larger fields for the same applied voltage. Secondly, high strain piezoelectric actuators are typically based on ferroelectric materials, in which the polarization state can be re-written by a sufficiently high electric field. In most cases, piezoelectric materials are driven in a unipolar fashion, such that the applied voltage is parallel to the remanent polarization induced by a prior poling step. When voltages exceeding $\sim 1/2$ of the coercive voltage are applied opposite to the remanent polarization direction, the material the piezoelectric begins to depole, degrading both the piezoelectric coefficient and the linearity of the response.[10] Thus, it is important not to drive the piezoelectric to large fields of the wrong sign. This is particularly critical in thin film devices, since large fields are induced by relatively small voltages. Thirdly, thin-film piezoelectrics on thick substrates show much lower levels of ferroelastic domain wall motion than piezoelectric ceramics and so tend to be less hysteretic than bulk actuators of the same composition.[11] However, with appropriate poling to minimize nonlinearity and aging, the responses can be very stable.

This work reports on the actuation capabilities of two TAO devices using optical metrology. Section 2.1 first discusses the design of the TAO devices including their fabrication. Next in Section 2.2, the optical metrology used to make interferometric measurements of devices is described. This is followed by a discussion of the control electronics and software used alongside metrology to actuate the devices (Section 2.3). Then in Section 3, the experiments to characterize the actuators of TAO devices are discussed including influence function measurements as well as linearity, hysteresis, and creep characterization. Finally in Section 4, the TAO devices are shown to measure the deflection of a laser using their actuators at both low and high frequencies.

2. TAO DEVICES

2.1 Mirror Design

Figure 1 shows the cross-section diagram of a TAO device and the materials used during fabrication. The substrate used was a 6 in. (152.4 mm) diameter, high temperature platinized silicon wafer. Platinized silicon wafers are commonly used in the fabrication of micro-electromechanical systems (MEMS)[12,13] and are desired for their adhesion, durability, and compatibility with MEMS stacks. The silicon (Si) portion of the substrate was 500 μm thick and included a 300 nm thick silicon dioxide (SiO_2) layer which acted as an insulator between the Si substrate and the titanium (Ti) layer. The 10 nm thick Ti layer served as an adhesion layer between the SiO_2 layer and the platinum (Pt) bottom electrode. The 150 nm thick Pt layer was the last layer in the platinized silicon wafer and served as the bottom electrode for the actuators fabricated on top of it. The Pt was sputtered at ~ 600°C to yield high density and strong {111} orientation.

Lead zirconate titanate (PZT) was used for the piezoelectric in the actuator stack. A commercially available $Pb(Zr_{0.52}Ti_{0.48})O_3$ sol-gel solution from Mitsubishi Corporation with 2% niobium (Nb) doping to decrease electrical conductivity was used to deposit the piezoelectric layer. An ~ 40 nm seed layer of PZT with a Zr to Ti ratio of 44/56 was first deposited to promote the {001} orientation. Each layer was then spin-coated, then exposed to an initial heating (~ 100°C) to remove solvent. It was then placed on a second hot plate at ~ 300°C for several minutes to pyrolyze the film.[14] The seed layer was then heat treated in a rapid thermal annealer at ~ 700°C to crystallize the PZT into the perovskite phase.

Next, the film was prepared by spin coating a layer of PZT with a Zr to Ti ratio of 52/48 to maximize the piezoelectric response ($e_{31,f}$ coefficient)[15] followed by similar heating, pyrolysis, and annealing steps. This process was repeated over 38 layers until a total film thickness of ~ 2.8 μm was achieved. X-ray diffraction was then conducted to verify that the primary film orientation was {001}, a crucial step for maximizing piezoelectric response in the direction shown in Figure 1.

After the PZT deposition, 3 nm thick Ti and 50 nm thick Pt layers were deposited using radio frequency (RF) magnetron sputtering to serve as the top electrodes in the actuator stack. The top electrodes were segmented into rectangles using a patterned photoresist and lift-off process. The top electrode deposition step was done in 6 rows across the wafer with each row corresponding to a unique number and size of top electrodes. Figure 2(a) shows the lithography mask design of the rows on top of the wafer. Row 2A of the wafer included 20

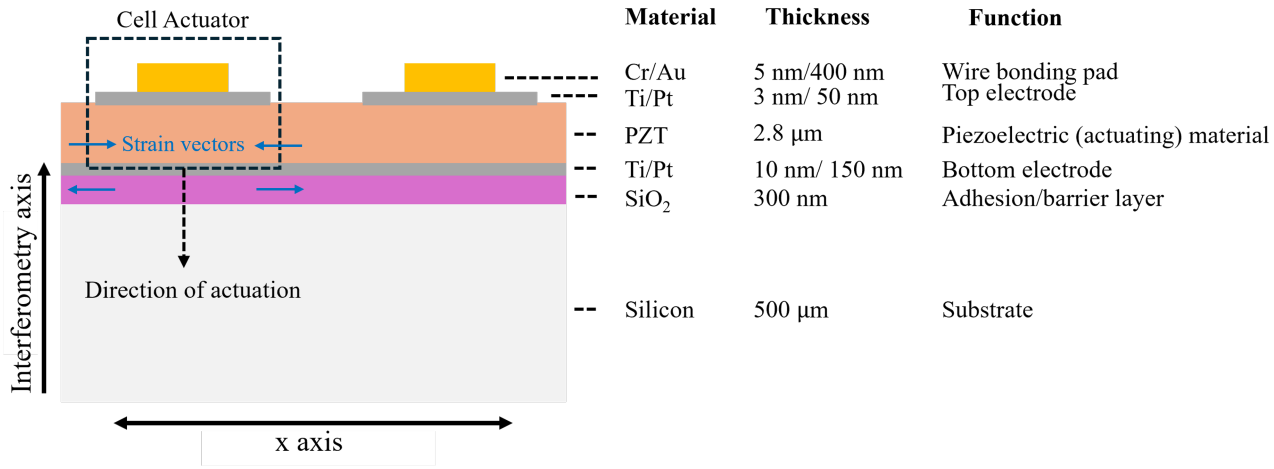

Figure 1. Cross-sectional diagram of a TAO device, including the materials used, their thicknesses, and function in the device. The combination of bottom electrode, PZT layer, and segmented top electrode and bonding pad form a discrete actuator, referred to as a "cell" in this work.

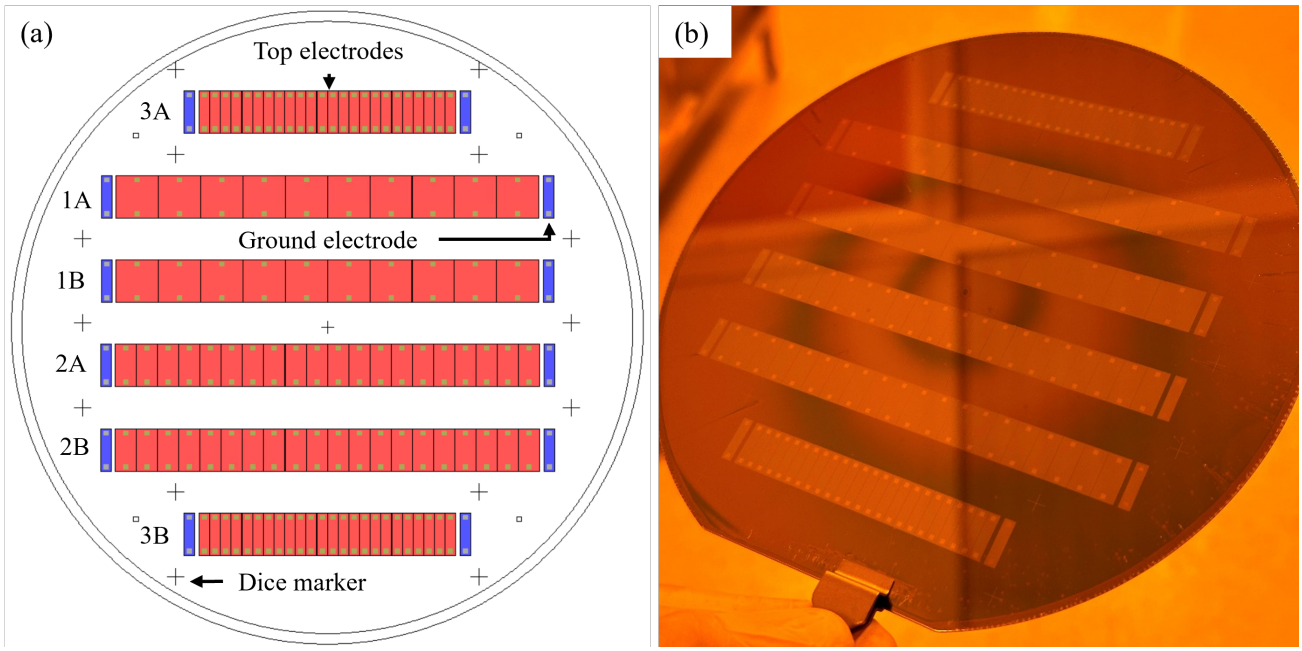

Figure 2. (a) Lithography mask design of the cell stacks on top of 152.4 mm diameter platinized silicon wafer. Each row was labeled according to its number of cells and individual cell size. (b) The wafer after the fabrication of cell stacks. The wafer was subsequently diced by row to form individual TAO segments.

top electrodes, each measuring 10 mm × 5 mm in size. Row 3A of the wafer included 24 top electrodes, each measuring 10 mm × 2.5 mm in size. The spacing between adjacent top electrodes was 40 μm.

The bottom electrode was then exposed using a photoresist and wet etching process. The photoresist was deposited and exposed to UV light through a mask to expose the regions of PZT designated for removal. Then a buffered oxide etchant was used to etch away the PZT followed by a cleaning using a combination of deionized water and hydrochloric acid to remove residues. Two bottom electrodes were exposed for each actuator row in the wafer, spaced 1 mm from both ends of the row.

After the bottom electrode exposure, direct current magnetron sputtering and negative photoresist patterning were used to deposit 5 nm thick chromium (Cr) and 50 nm thick gold (Au) pads onto the top electrodes. Two

pads were deposited per top electrode and serve as wire bonding points to connect the actuators to their control electronics. As shown in Figure 1, the combination of wire bonding pad, top electrode, PZT layer, and bottom electrode form a discrete actuator on the optic and are hence referred to as a "cell" in this work. Figure 2(b) shows the wafer after cell fabrication. After completion of the cell stacks, each fabricated row was diced using alignment markers on the wafer, with the exception of row 3A, which was cleaved manually. Each diced row represents a segment of the initial wafer and hence the six TAO devices fabricated from a single wafer were labeled according to their segment. This work reports on the progress of Segment 2A and Segment 3A. The crystallization of the PZT during cell fabrication tends to produce a tensile stress on substrates due to their mismatch in coefficients of thermal expansion.[16] In the context of thin-film PZT adaptive optics this stress can induce significant mirror surface deformations[8] that can be corrected for through a stress compensation step. In these initial experiments for these prototypes, no stress compensation was employed.

Figure 3 shows the fabricated TAO segments. TAO Segment 2A measured 20 mm × 115 mm in total and consisted of 20 cells of size 10 mm × 5 mm. TAO Segment 3A measured 20 mm × 80 mm in total and consisted of 24 cells of size 10 mm × 2.5 mm. The TAO devices were laid face down onto a set of perforated boards (perfboards) so that they could be wire bonded. This means that the front side of the segments could not be measured during mirror operation. However, the metrology methods described in Section 2.2 still allowed for measurement of the total mirror figure and figure change induced by cells, albeit negative to the orientation typically used for adaptive optics. The mirrors were secured to the perfboard using Kapton tape around the perimeter of the segments.

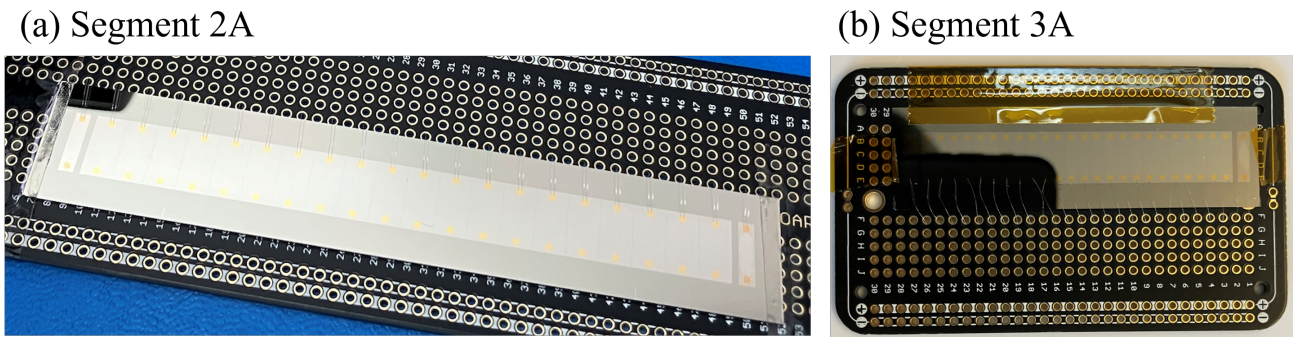

Figure 3. Pictures of the fabricated TAO devices (a) Segment 2A and (b) Segment 3A. The segments were placed face down onto a pefboard. The gold contact pads of each segment were wire bonded to the perfboards and the segment edges were secured with Kapton tape. Segment 2A consists of 20 cells, each measuring 10 mm × 5 mm in size. Segment 3A consists of 24 cells, each measuring 10 mm × 2.5 mm in size. Both segments include 2 bottom electrode pads located at either end of the segments which serve as electrical ground.

The realized TAO cells utilize the converse piezoelectric effect of the PZT to induce localized deformations on the optic. More specifically, when a DC voltage is applied between the top and bottom electrodes of a cell, the electric field generated produces a biaxial inward strain in the x and y dimensions within the PZT film. The net effect of these strains bends the substrate toward the mirror surface as shown in Figure 1. The magnitude of the strain produced is proportional to the voltage set and hence the sum of localized cell deformations can induce a net figure change across the optic. With proper measurement of individual cell responses and the initial figure of the mirror, the voltage for each cell can be calculated to produce a figure change that corrects the mirror figure.[17] Additionally, given an arbitrary target surface wavefront shape, cell voltages can be similarly calculated to realize the shape.

2.2 Optical Metrology and Mirror Figure

Figure 4 shows the metrology setup used to measure the figure of the TAO segments. A 4D Technology AccuFiz H100S Fizeau interferometer with a 6 MP camera was used for measuring the surface heights of the TAO segments. An aperture converter was used to convert the interferometer's native 4 in. (101.6 mm) aperture to 6 in. (152.4 mm) to capture the full area of TAO segments. An attenuating transmission flat with a surface

error of $\lambda/20$ ($\lambda = 632.8$ nm) was installed to the end of the aperture converter. The transmission flat produces a high quality, planar reference wavefront which is both transmitted to the optic being measured and reflected back to the interferometer camera. The TAO devices were mounted into a manual alignment stage. With proper alignment of the transmission flat and optic being measured, the interferometer computes the difference between the reference wavefront and the wavefront reflected off the test optic to produce a fringe map of the optical surface. This fringe map is then integrated to produce a figure map of the optic.

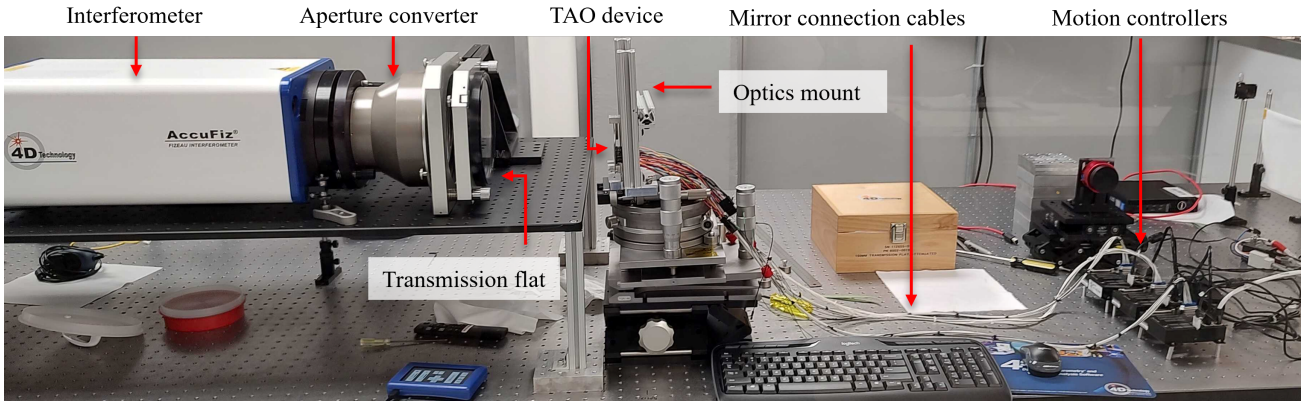

Figure 4. Optical metrology setup used by UI to measure TAO segments' surface figure. This setup was also used to measure the figure change induced by cell actuation and included connections between segments and the motion controllers.

Typically, Fizeau interferometers gather measurements using the temporal phase-shifting interferometry (TPSI) method. In TPSI, several frames are captured sequentially, wherein the reference wavefront path is phase-shifted between frames (typically by 90 degrees) which allows the interferometer to unwrap the phase at each point in the image and solve for the mirror surface height. However, if substantial vibration is introduced between phase shifts, it can cause errors that are too great to reliably solve for the phase.[18]

Though measurements were performed on a vibration-isolated, laminar flow workbench inside an ISO 7 clean room environment, the elevated metrology setup combined with the cavity distance between the transmission flat and test optic can produce systematic measurement errors. Thus, measurements of the TAO segments were made using a dynamic measurement method.[19] In dynamic operation. a linear spatial phase shift is induced across the camera pixels by offsetting the reference wavefront from the test wavefront by tipping the transmission flat at a slight angle (< 0.5 degrees). A convolution algorithm is then used to parse the interferogram from the phase-shifted pixels. The benefit of this method is that data can be captured in a single frame as the phase-shift is occurring spatially instead of temporally. The accuracy of this method was further improved by averaging over 50 measurements per figure map produced when measuring the TAO segments.

Figure 5 shows the initial figure maps of TAO Segments 2A and 3A. A detector mask was applied during measurements to exclude the figure around the perimeter of the segments. This was done for several reasons. The first is that the edges of the segments introduce vignetting and a drop of fringe contrast making measurement of the figure at the edges unreliable. The second is that, as stated in Section 2.1, the perimeter of the segments were overlaid with tape to secure them to their perfboards. These regions produce unreliable interferograms due to the low optical quality. In Figure 5(b), an additional mask was applied to the top of Segment 3A to filter out a region of tape. Finally, in a practical use case, the edges of an X-ray optic are typically reserved as mounting points and do not contribute to the focusing of X-ray beamlines.

For Segment 2A, the root mean square (RMS) figure error was 6.35 μm and the peak-to-valley (PV) figure error was 25.87 μm. For Segment 3A, the RMS error was 1.92 μm and the PV error was 7.58 μm. The greater PV reported for Segment 2A over Segment 3A was attributed to its longer mirror length. The peak-to-valley reported in Figure 5 represents the robust peak-to-valley (PVr) of the figure map. The PVr is defined as the simple peak-to-valley of fitting the figure map to a 10th order Legendre fit in both the x and y dimensions plus three times the RMS of the difference between the original figure map and the fit. The PVr metric gives a more

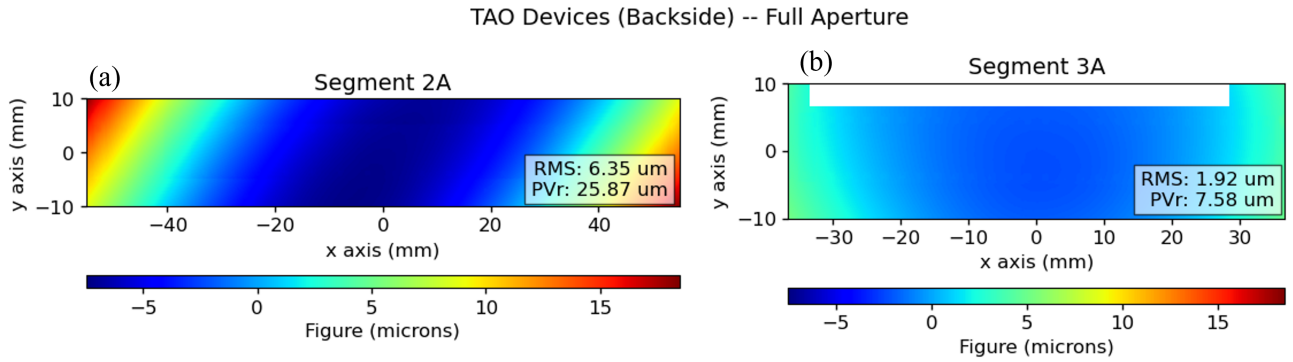

Figure 5. Figure maps of TAO (a) Segment 2A and (b) Segment 3A. The rectangular area of data omitted at the top of Segment 3A corresponds to the location of the Kapton tape used to secure the mirror to the perfboard. The RoCs for Segments 2A and 3A were 57.99 m and 86.70 m, respectively.

accurate representation of the true PV of the mirrors since it attempts to recreate the mirror figure first and is not as sensitive to outliers as the simple PV.

The corresponding radii of curvature (RoCs) for Segments 2A and 3A were 57.99 m and 86.70 m, respectively. The RoCs were calculated by fitting the figure maps of Figure 5 to a 2nd order Legendre fit both in x and y dimensions. The PV of these quadratic fits can be interpreted as the magnitude of sag of each segment from a flat shape. In the limit where the RoC is large compared to the diameter of the optic, the sag can then be used to solve for the RoC using:

$$S \approx \frac{D^2}{8R}, \tag{1}$$

where S is the sag in meters (obtained from the PV of the quadratic Legendre fit), D is the diameter of the segment in meters (taken from the length of the longer dimension of the mirror), and R is the RoC in meters. The large PV errors and subsequently small RoCs measured for Segments 2A and 3A mean that their magnitude of actuator deflection will be small compared to their initial surface figure. This means that even through the application of all cells, TAO Segments 2A and 3A will be unable to realize a figure correction that produces an ideally flat mirror. Likewise, they will also be unable to produce a wavefront shape that is not dominated by their surface figure error. However, a stress compensating film of SiO_2 can be applied to one side of TAO segments to reduce surface PV errors to within the range addressable by cells. Models of depositing compressively stressed SiO_2 on curved thin-film PZT adjustable mirrors has been shown to reduce PV figure errors to $\lesssim 0.1$ μm.[20] The process for stress-balancing future flat TAO segments is currently in development.

Additional measurements of TAO Segments 2A and 3A were made to calculate the RMS and PVr repeatability of the metrology setup described in this section. While the marketed RMS repeatability of the AccuFiz H100S Fizeau interferometer used is 0.03 nm,[21] this was reported when measuring a calibration mirror with a surface flatness of $\lambda/20$ when using TPSI. Given that the interferometric measurements presented in this work were made in dynamic operation, the presence of external vibration introducing systematic errors, and test optics with surface flatnesses of $\sim 41\lambda$ and $\sim 12\lambda$, a more accurate representation of the metrology error was needed. The following steps outline the method used to measure the RMS and PVr repeatability for the TAO segments:

1. Align the segment in the configuration shown in Figure 4.
2. Take 10 measurement sets. Each measurement set consists of 50 measurements (500 measurements total).
3. Compute the average figure map for each measurement set (10 averaged figure maps).
4. Compute the RMS and PVr for each averaged figure map (10 averaged RMS values and 10 averaged PVr values).

5. The RMS repeatability is calculated as the standard deviation of the 10 averaged RMS values.

6. The PVr repeatability is calculated as the standard deviation of the 10 averaged PVr values.

For Segment 2A, the RMS repeatability was 0.58 nm and the PVr repeatability was 2.35 nm. For Segment 3A, the RMS repeatability was 0.57 nm and the PVr repeatability was 6.38 nm. The mean measured RMS repeatability was approximately ~ 19 larger than the marketed repeatability. Given the difference between the parameters used to compute the two RMS metrics, another factor was the mounting of the TAO segments. While the optical stage provided a stable mount for measured optics, the TAO segment was taped to a perfboard that was inserted into the stage. This created a looser bond that would cause a slight drift in the alignment of the segment over time. This was evident when looking at the delta figure maps between repeatability measurements that demonstrated a linear shift predominately in y direction.

2.3 Control Electronics

A control system was designed to individually actuate cells to measure their figure change response. The RIO-47142 is a programmable logic controller commercially available from Galil Motion Control. In addition to the convenience afforded by using an off-the-shelf solution, each motion controller includes 8 analog inputs and outputs that operate on a range of ± 10 V_{DC} with 16-bit resolution. This range met the 0–10 V operational requirement commonly used in thin-film PZT X-ray mirrors.[9,22] Another benefit to using these controllers is their scalability. As described in Section 2.1, TAO Segment 2A included 20 cells and Segment 3A included 24 cells. Adjacent motion controllers can be connected to one another via their onboard dual-ethernet ports, meaning multiple controllers can be linked together to control an optic with an arbitrary number of cells.

A Python programming package called *axroGalil*[23] was developed to easily interface between a number of controllers and the 4D interferometer to allow for automation of actuation measurements of TAO segments after alignment. This software not only automates measurements but independently tracks the connections between analog inputs/outputs of controllers and their assigned cell within a user-defined adaptive optic. This made swapping of different TAO segments quick and tracking of metrology data products easily accessible.

Figure 6 shows diagrams of the user-defined cell layout for TAO Segments 2A and 3A, and their corresponding controller IDs. The cell numbering was defined from left to right when viewing the segments from the side connected to the controllers. Note that at the time of measuring Segment 3A, the University of Iowa (UI) metrology lab was in possession of only 2 motion controllers and thus controller 1 was swapped between controlling cells 1–8 and 17–24. Mirror connection cables were constructed (Figure 4) to connect the segment perfboards to the controllers. Tests were then performed on both segments to ensure electrical continuity of the voltage read and write capabilities to each cell.

Prior to interferometric measurement of cell responses, both TAO segments were poled at room temperature and at 10 V for approximately 30 min. Poling serves to produce a remanent polarization by aligning the domains of the PZT. The result is that the cells will produce a large, repeatable strain within the PZT,[24] ensuring operability of the TAO devices. The TAO segments were poled at 10 V due to the voltage limitations of the control electronics. However, poling is typically done above the nominal operation voltage to produce a stronger net polarization. Typical poling parameters for thin-film PZT actuators of this type include heating the film to (125°C–150°C) at three times the coercive voltage (160 kV/cm–180 kV/cm).[25] Thus, the PZT films were not completely polarized. This had implications for the non-linearity and creep observed in these prototypes described in Sections 3.2 and 3.4.

In the future, the segments will be repoled at a higher voltage and elevated temperature. Hot poling can achieve further net polarization[26] by increasing the mobility of dipoles within the PZT via an increase in thermal energy. Hot poling has also been shown to reduce hysteresis in the strain response and reduce aging rates.[17]

3. CELL CHARACTERIZATION

3.1 Influence Function Measurements

For a thin adaptive optic, an influence function (IF) is the figure map produced from measuring the figure change of a single actuator at a set voltage. To measure an IF of a TAO segment, an initial reference measurement

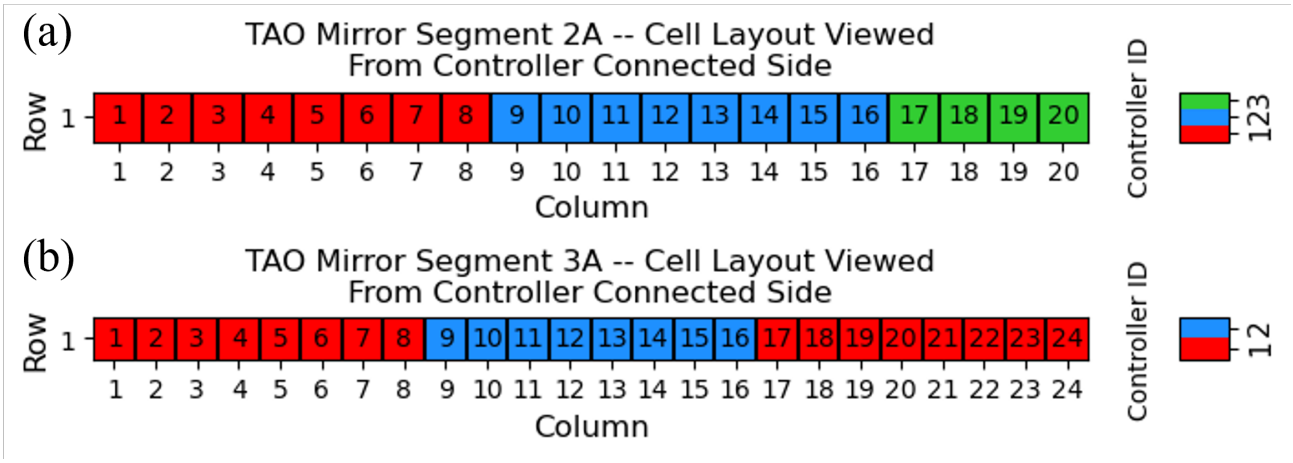

Figure 6. Diagram of the cell layout and numbering for TAO (a) Segment 2A and (b) Segment 3A. The layout is viewed from the controller connected side of the segments (the side not facing the interferometer). Cells 1–8 and 17–24 of Segment 3A were controlled by swapping the connection of a single controller.

is made of the mirror surface (like the ones shown in Figure 5). Then a single cell on the segment is set to a constant voltage and another measurement of the surface is made. The IF for that cell is the result of the reference measurement subtracted from the actuated measurement. The set of IFs for all cells in a segment form a basis set of functions that, when scaled individually and summed together, represent a net figure change across the mirror. In this case, the scale factor for each IF represents the voltage of each cell to induce the net figure change. Thus, in order to calculate the cell voltages needed to either correct for mirror distortion or to form a target wavefront shape, the IFs of a TAO device must be measured.

The IFs of Segments 2A and 3A were measured using an actuation voltage of 10 V, limited by the maximum voltage of the motion controllers. The segments were aligned as shown in Figure 4 and IF measurements were automated using the software described in Section 2.3. The segments were masked in software to only measure the area covering the cells of both segments. A measurement was made of a segment with all cells set to 0 V, then a cell would be set to 10 V and the segment remeasured before proceeding to the next cell. The grounded figure maps were then subtracted from their corresponding actuated figure maps to construct the IFs of both segments.

By way of an example, Figure 7(a) shows the measured IFs of cells 3 and 10 of Segment 2A. Figure 7(b) shows the measured IFs of cells 3 and 10 of Segment 3A. Included in the IF figure maps are the RMS and Q percent peak-to-valley (PV_Q) of each IF. The PV_Q is defined as the simple peak-to-valley of the middle Q percent of data when arranged on a histogram (90% in the case of Figure 7). The PV_Q is the second preferred PV metric after the PVr for filtering outliers in a data set that cannot be well fit by a small number (≤ 10) of Legendre polynomials. The reason for using PVr in initial optical surface (Figure 5) versus using PV_Q for IFs (Figure 7) has to do with whether absolute or relative figure is being measured. The absolute figure of most manufactured optics can be described by low order (≤ 10) terms due to surface error occurring over low spatial frequencies. An IF, however, represents a relative figure change between initial figure and figure after actuation. Thus, IF maps contain higher spatial frequencies that would require many higher order terms to accurately describe the data. Thus, the PV_Q is used as a computationally fast way to measure the peak-to-valley while excluding outliers. In Figure 7, the bumps of each IF appear as valleys because the direction away from the interferometer is processed as negative data, and the TAO segments were mounted with cells actuating along this orientation.

There are several visible patterns in the measured IFs of Figure 7 that are related to the design of the TAO segments. The first is that the IFs of Segment 2A had a larger bump area than IFs of the same cell number in Segment 3A. This is due to the cell width of Segment 2A being twice as wide as that of Segment 3A (5 mm vs. 2.5 mm). The next pattern is that, for the same cell number, the PV_Q of the IF of Segment 2A is larger than the PV_Q of the IF of Segment 3A. Despite using the same voltage, this is due to Segment 2A being longer than

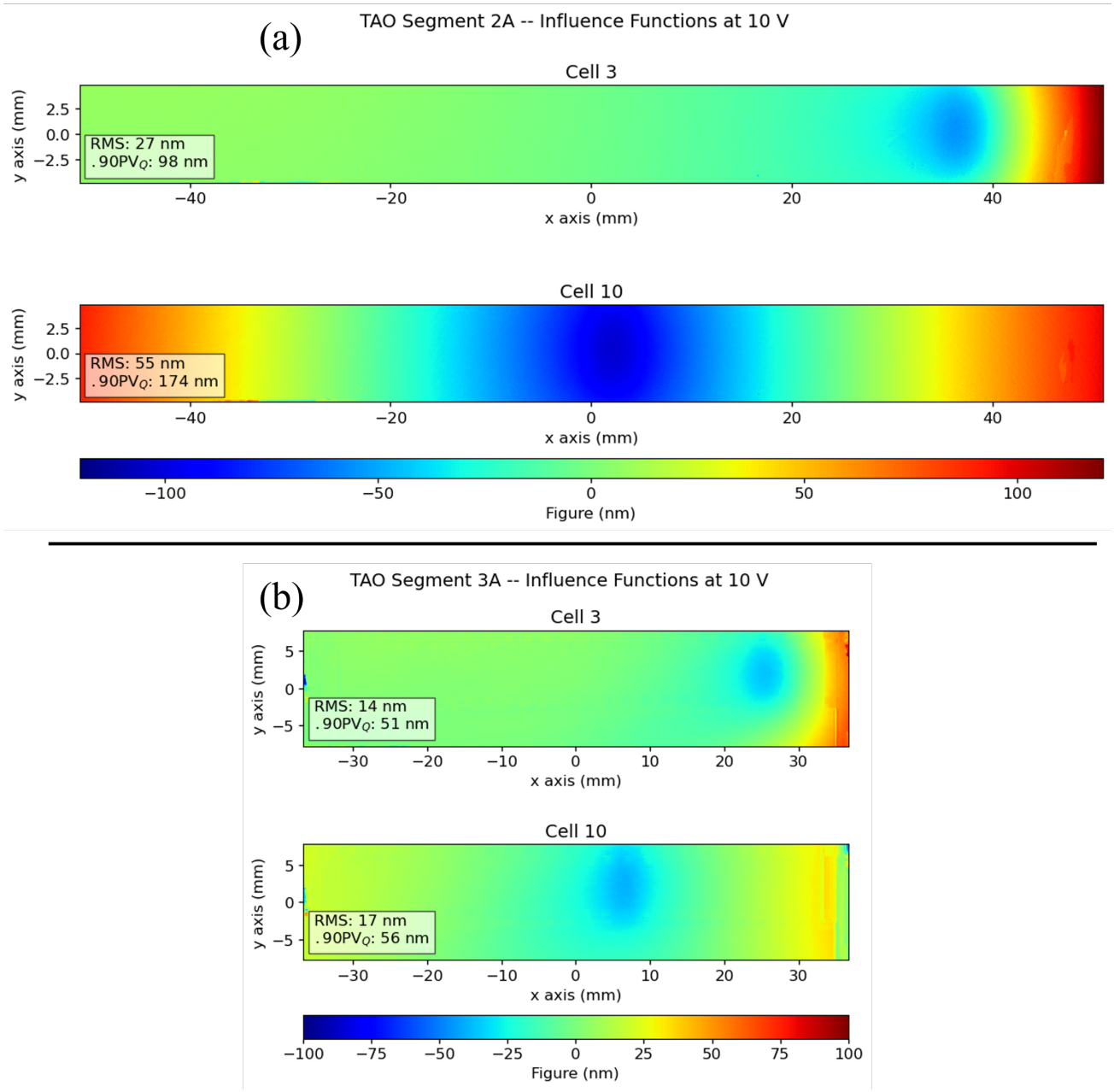

Figure 7. IF measurements of TAO (a) Segment 2A and (b) Segment 3A made at 10 V. The figure maps show measurements of a cell near the edge of the mirror (cell 3) and the middle of the mirror (cell 10). Note the change in color bar scale between figures (a) and (b).

Segment 3A (115 mm vs. 80 mm). A longer segment affords a larger bending moment in the optic, resulting in a larger surface deformation. This geometric constraint is also related to the third pattern shown in Figure 7: for the same segment, the IF of a cell near the center of the segment (cell 10) had a larger PV_Q than a cell near the edge of the segment (cell 3). The reason for this is described by the Kirchhoff-Love model of out-of-plane displacement for a thin plate under a transverse load. For a plate constrained at the edges, the largest deflection will occur at the point furthest from the constraints: the geometric center of the plate.[27] As described in Section 2.1, both segments were constrained to perfboards using tape around the perimeter hence the larger actuation observed at the center is expected. This effect is enhanced as the area of plate increases, hence the larger increase

in PV going from side IF to middle IF for the longer Segment 2A than the shorter Segment 3A.

After measuring the IFs of both segments, the two-dimensional figure maps were averaged along the y dimension to produce a set of one-dimensional (1D) IFs. This was done as the segments are only intended to induce slope changes along a narrow band in the x dimension when aligned with an X-ray beam. Figure 8 shows the measured 1D IFs of Segments 2A and 3A. On average, the IFs of Segment 2A were able to induce a PV_Q of 183 nm and the IFs of Segment 3A induced a PV of 63 nm. Note that the edges of the 1D IFs of Segment 3A (Figure 8(b)) show spikes in the figure data. This is due to the detector mask of Segment 3A being set just outside the top electrode region on either side of the segment which resulted in a drop-off in figure reconstruction due to the steep discontinuity in mirror surface height.

As shown in Figure 8(a) all IFs of Segment 2A were successfully measured, resulting in 100% cell yield for the optic. For Segment 3A, IFs for cells 1, 2, 4, 7, 18, and 20 could not be observed due to failures in the wire bonding used to connect the gold pads of the segments to the perfboards; For the cells whose IFs were not observed, the wirebonds between the gold contacts on the segments and wires connecting them to the perfboard detached. The current wire bonding method presented in this work represents a solution for quickly wiring prototyped segments but does not afford long-term operability; a more robust method of connecting TAO devices is currently in development.

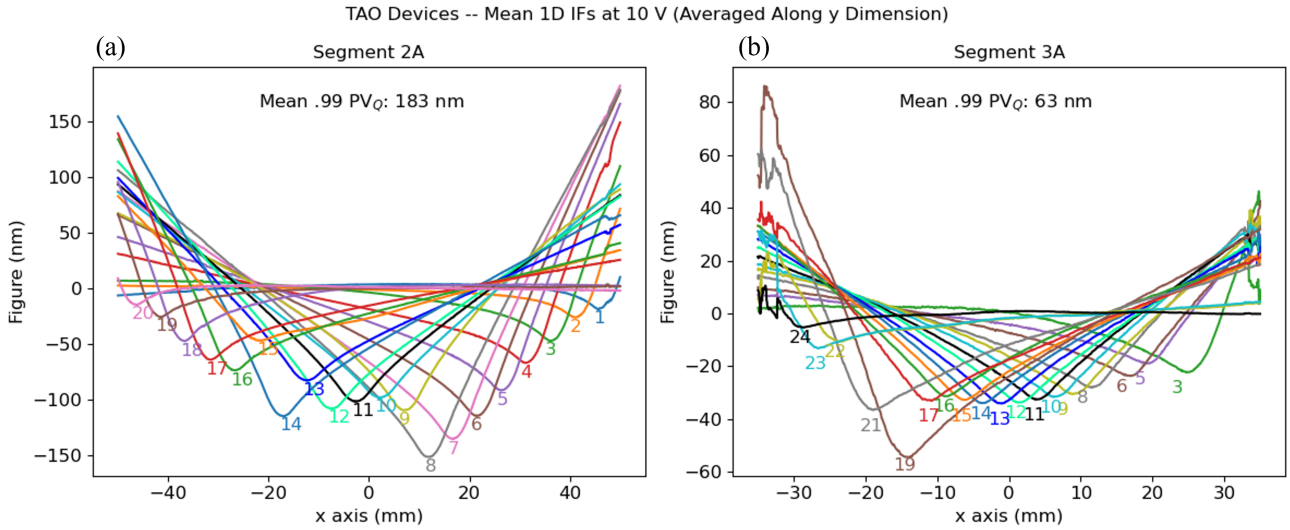

Figure 8. 1D IF measurements averaged along the y dimension for TAO (a) Segment 2A and (b) Segment 3A at 10 V. The colored numbers index the cell number corresponding to each IF using the layout illustrated in Figure 6. Note the change in figure scale between the two plots.

3.2 Cell Linearity Characterization

The response of cell 12 of Segment 3A was measured to test if the IF figure change magnitude increased linearly with voltage. This attribute of cell response is of particular interest in TAO devices since the matrix inversion method typically used for figure correction in PZT optics assumes a linear scaling of the IF with voltage. The net figure change is computed as a dot product between voltages and IFs.[9] If the measured IF scaling deviates significantly from a linear trend, then it is likely that the matrix inversion model will not accurately predict the wavefront shape, requiring a more nuanced method. It was expected that the actuation response would not be completely linear due to incomplete poling.

To test for linearity, a series of IFs were measured for cell 12 with the actuation voltage increasing from 0 V to 10 V in 1 V increments. Figure 9(a) shows the measured mean 1D IFs for the range of actuation voltages. The x axis extent of the IF measurements was windowed to center closely around the bump of the IF. The "peak" of each IF represents the minimum value of the IF since the actuation direction was opposite the side of the interferometer. The exception to this was the 0 V measurement in which case the maximum figure point was

taken. The IFs showed good alignment of the peak figures in the x dimension, indicating that the direction of actuation remains perpendicular to the optic surface with increasing voltage.

The peak figure and corresponding actuation voltage of each IF were then plotted in Figure 9(b). A linear and quadratic polynomial fit was applied to the set of peak figures. The quadratic model ($R^2 = 0.99$) provides a slightly better fit to the peak figure than the linear model ($R^2 = 0.95$). This result suggests that the cell response is not entirely linear. The fact the IFs shown in Figure 9(a) appear symmetrical and well aligned suggests that the cause for the non-linearity is not due to fringing fields as a result non-uniform electrode coverage.

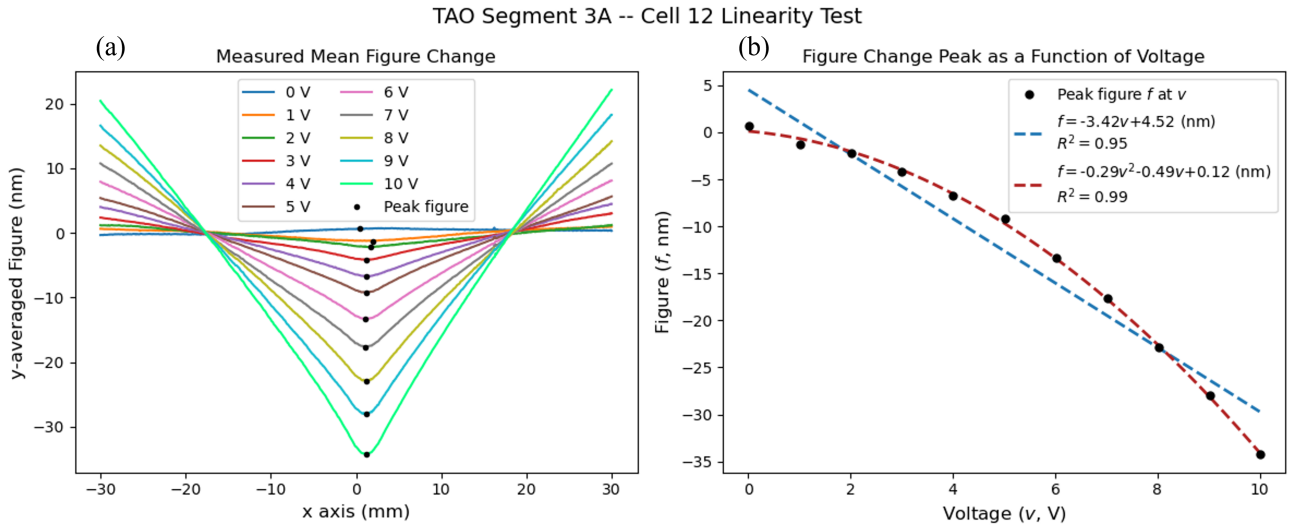

Figure 9. Cell 12 actuation linearity test of TAO Segment 3A. (a) The measured mean 1D figure change between a 0 V interferometric measurement and a measurement made when Cell 12 was set to 0–10 V. The "peak" of each figure change refers to the lowest point in the actuation profile since the direction of actuation on the segment was opposite the direction of the interferometer. (b) The peak of each figure change map in (a) plotted as a function of the cell voltage. The cell actuation response is better described using a quadratic model than a linear model.

The likely reason for the observed non-linearity was the presence of a ferroelectric hysteresis in the PZT wherein the figure of the IF at the actuation voltage is dependent on the voltage that the cell was previously set to. More specifically, a significant amount of the domains within the film remained non-aligned with the field orientation as a consequence of incomplete poling. Thus, as the voltage was increased, the film underwent domain switching which yielded a non-linear response. The IFs measured in this test had cell 12 repeatedly set to 0 V in between being set to the actuation voltage in order to make the reference ground measurement to construct the IF. Thus, each time cell 12 was set to a larger actuation voltage, it is likely that a larger volume of domains switched to generate the quadratic figure change seen in Figure 9.

Domain switching occurs through a process of domain nucleation and growth, and is exacerbated when the applied voltage exceeds the coercive voltage (V_c). Typically, domain nucleation begins at fields of approximately 1/2 the coercive voltage. Because the range of voltages at which that the linearity test was conducted is near the coercive voltage for the PZT films of the TAO devices, non-linearity is expected in the partially poled PZT film as a result of domain switching. That is, the observed strain includes both the piezoelectric responses and poling strains, which increases the nonlinearity.[28] However, the observed linearity shown in this work is likely sufficient for using the matrix inversion model to perform wavefront shaping. It is important to note that adjustable optics that underwent room temperature poling demonstrated cell responses that were predicted using a matrix inversion model using a thinner piezoelectric film.[9]

3.3 Cell Hysteresis Characterization

As a follow up to the linearity test discussed in Section 3.2, a simple test was conducted on cell 12 of Segment 3A to investigate the presence of hysteresis when alternating between the ground state and the actuation state.

Five measurements were made of cell 12 at varying voltages without the use of successive reference measurements in-between. First, cell 12 was set to 0 V, then 10 V, then 0 V, then -10 V, and finally 0 V. It is important to note that since the devices were poled at 10 V, it was expected that -10 V actuation would cause a partial repoling of the PZT opposite to the original field direction. Furthermore, since the -10 V and 10 V states were near the coercive voltage of the film, hysteresis of the stress response was also likely. Mean 1D IFs were constructed of the -10 V and 10 V measurements using the 0 V measurements that preceded each. Figure 10(a) shows all the measurements for this test. The IFs for the -10 V and +10 V states were then differenced, which is shown in Figure 10(b). The difference in IFs showed a PV of 14 nm. This metric is significant given that this PV represents $\sim$ 22% the PV of the cell 12 IF shown in Figure 8(b) and is above the 6.35 nm PVr repeatability reported for Segment 3A in Section 2.2.

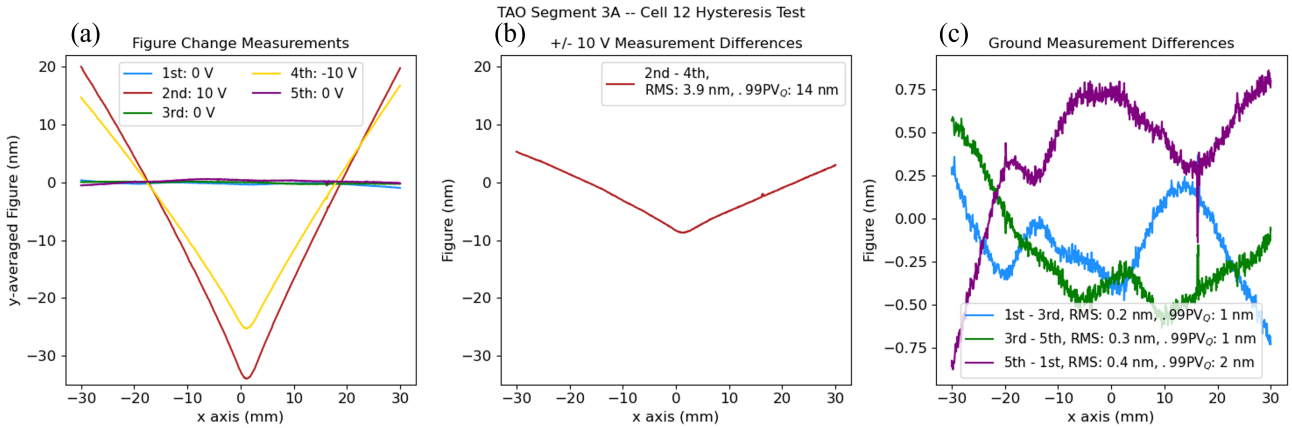

Figure 10. Cell 12 actuation hysteresis test of TAO Segment 3A. (a) The measured mean 1D figure change between a 0 V interferometric measurement and a measurement made when Cell 12 was set to 0, -10, and 10 V. The legend denotes the order the measurements were taken in. (b) The difference between the +10 V and -10 V measurements shown in (a) which illustrate a figure difference of 14 nm PV when returning to 0 V in-between measurements. Thin-films are more susceptible to domain switching under bipolar field applications, which can result in a significant difference in actuator response. (c) The difference between the set of 0 V measurements shown in (a). The average figure difference was $\sim$ 1 nm PV when actuating to +/-10 V between measurements, which is indicative of metrology error since it is within the 6.35 nm PVr repeatability described in Section 2.2.

This disagreement is not explained by a disagreement in the 0 V reference measurements for each IF as Figure 10(c) shows the difference between the 0 V measurements. The disagreement between 0 V measurements is much smaller and indicative of metrology error and is not structured by cell behavior. These results suggest a hysteresis of cell response when alternating between the 0 V and $\pm$10 V states. This result shows that the actuation repeatability of thin-film piezoelectrics is limited for bipolar voltage applications since the film is more likely to domain switch upon reversal of the field for applied voltages near the coercive voltage. As is widely known, piezoelectric materials should not be driven at $>$ 1/2 the negative coercive field, especially with DC voltages, to avoid depoling the part.

However, it is not expected that the observed hysteresis is likely to affect the ability of these devices to perform wavefront shaping or figure correction. In the case where negative slope changes are more commonly needed in the application of these optics, a small, positive DC bias can be applied to all cells. This would induce a global figure change across the mirror, from which cell voltages can be decreased toward 0 V to generate local negative slope changes.

3.4 Cell Creep Characterization

Another test was conducted to study the amount of creep demonstrated by a cell undergoing prolonged actuation. "Creep" in this context refers to the stability of a cell to sustain its local deformation when kept at a constant voltage. It is important to note that since the TAO segments were not completely poled, then prolonged actuation would serve to improve the domain alignment over time. Thus, it was expected that some amount of creep would

be measured over the duration of this test. While creep is not as direct of a concern during high frequency beam pointing applications, it is relevant to static applications of PZT actuators for maintaining precise optical figure. To test for creep, an initial measurement was made of Segment 3A with all cells grounded. Then, cell 12 was set to 10 V for ~ 30 min, with interferometric measurements made approximately once a minute. IFs of cell 12 were then constructed by subtracting the initial ground measurement from all subsequent timed 10 V measurements.

Figure 11(a) shows the IFs from the beginning and end of the test ($\Delta t = 28.58$ min). Over the duration of the test, the IF of cell 12 showed an overall increase in figure change magnitude, with the largest portion of the increase occurring at the peak of the bump of the IF. This is more clearly shown in Figure 11(b), which illustrates the difference between the IFs at the start and end of the test. The residual is structured such that the difference between measurements is not due to optical misalignment over time. Instead, there was slight sharpening of the actuation profile that produced an ~ 1 nm figure change PV. However, it is worth noting that the ~ 1 nm figure change observed fell within the 6.35 nm PVr repeatability measured for Segment 3A, placing this change on the level of the metrology noise.

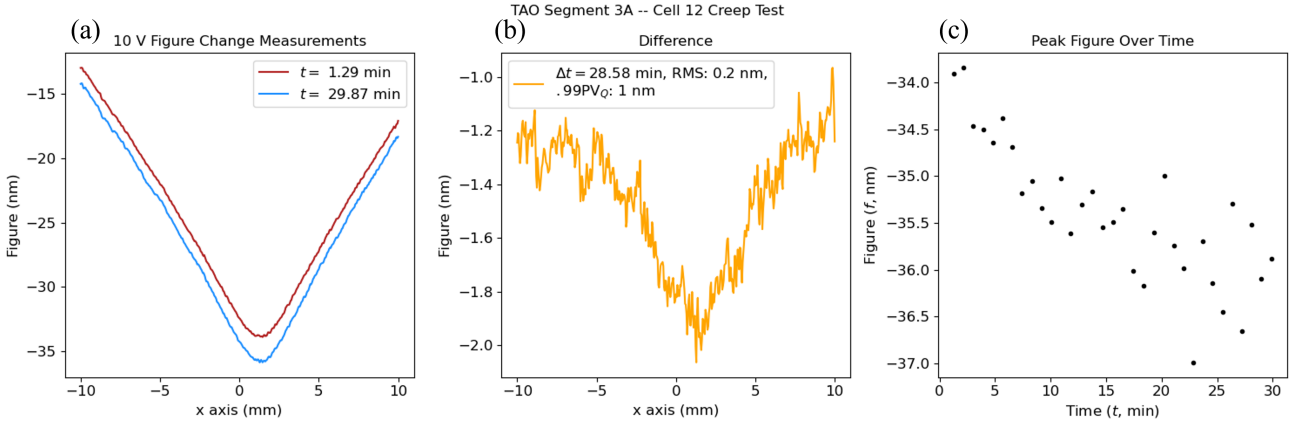

Figure 11. Cell 12 actuation creep test of TAO Segment 3A. (a) The measured mean 1D figure change between a 0 V interferometric measurement at $t = 0$ min and a measurement made at 10 V at $t = 1.29$ min and $t = 29.97$ min. (b) The difference between the figure change measurements shown in (a), which resulted in a < 1 nm change, peak-to-valley. (c) The peak of each figure change measurement plotted as a function of time. The "peak" of each figure change refers to the lowest point in the actuation profile since the direction of actuation on the segment was opposite the direction of the interferometer.

For each measurement in this time series, the peak figure was extracted and plotted in Figure 11(c). The peak figure appears to gradually increase for $t < 6$ min, before becoming more erratic over time. The measured creep PV represents 1.5% of the PV of the cell 12 IF measured in Figure 8(b) and is on the level consistent with metrology error. Though currently the TAO cells show creep below metrology error during prolonged use, the PZT actuation stability can be further enhanced through hot poling the PZT film.

4. LASER DEFLECTION EXPERIMENTS

The ultimate purpose for TAO device development is to focus X-ray beamlines. Though optical metrology serves to characterize the performance of TAO cells, the ability to repeatably steer beam direction is a desired attribute of these optics. Thus, experiments were conducted using TAO Segment 3A to demonstrate the repeatable deflection of a laser. Figure 12 shows the setup used to perform these experiments. A spatial filter pinhole was placed in front of an optical laser ($\lambda = 635$ nm) to filter higher-order spatial modes and allow the Gaussian mode to pass through. The beam then passed through a focusing lens before reflecting off of two flat mirrors. The combination of tip and tilt adjustments between the two mirrors allowed the beam to be steered in x and y independently to reflect off a precise location on the TAO device. After reflecting off the two mirrors, the beam passed through a vertical slit to limit the x divergence of the beam. The width of the slit was also adjusted to allow the laser to reflect off of one or several of the TAO cells before reaching a camera. The camera used was a ASI6200 MC Pro,[29] which has a resolution of 9576×6388 pixels and a pixel size of 3.76 μm.

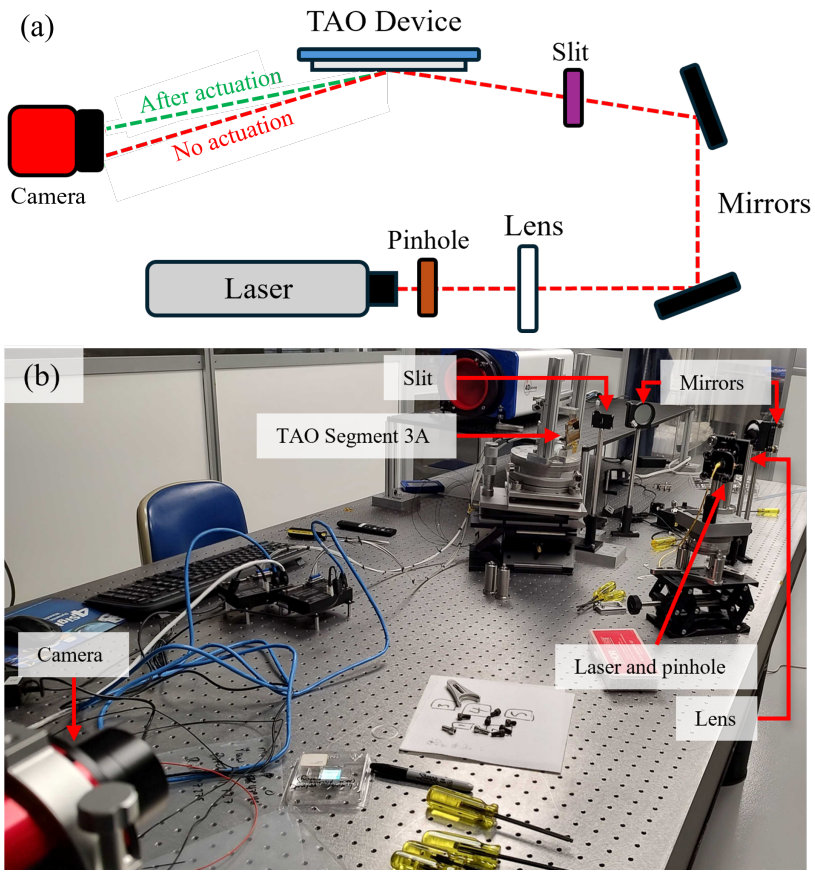

Figure 12. (a) Diagram of the setup used to measure laser deflection driven by TAO cell actuation. (b) Picture of realized experimental setup. In this picture, TAO Segment 3A was connected to the motion controllers used during interferometric measurements for discrete deflection testing. The segment was later connected to a function generator in this same configuration for high frequency deflection measurements.

When one or several cells on the TAO segment are actuated, the beam path reflecting off the segment is deflected in the x dimension. The laser position on the camera for each frame captured was calculated using the centroid intensity of the beam. Using the setup in Figure 12, the laser centroid was tracked without cell actuation to measure the uncertainty in x position. The standard deviation in x position was ± 0.3 μm, which was attributed to vibrational instabilities in the measurement setup.

Initially, cells were controlled using the motion controllers discussed in Section 2.3 to perform discrete (on/off) actuation. This was performed to observe repeatable deflection at low driving frequency. This frequency regime (0.01 Hz–1 Hz) is of interest for preserving optical figure[30] and to quickly change beam profile to accommodate sample switching.[31] TAO Segment 3A was later connected to a function generator to repeat the experiment while driving cells at higher frequency, which is useful for applications where bright beams are intentionally decohered (100 Hz–100 kHz).[32]

The first test measured laser deflection off of cell 12 of TAO Segment 3A driven by discrete 10 V actuation over a 1 second cycle. It is important to note that for the discrete actuation test, while the voltage was programmed to a 10 second hold between voltage states, the true driving period was slightly larger given the added execution time for Python to set and read voltages using the *axroGalil* package. The camera frame rate was set to 26 ms per frame during this test, which was negligible compared to the cell actuation cadence.

Figure 13 shows the laser centroid position on the camera for each frame captured during the test. The plot shows two clusters of centroid locations, with points at $x < -0.48$ μm corresponding to the 10 V state of the cell and points at $x > -0.48$ μm corresponding to the 0 V state. The mean position for both states was calculated

and show an average deflection distance of 4.33 μm. The x position of the centroid locations shown in Figure 13 were then extracted and plotted as a time series in Figure 14. The laser shows a clear oscillation of x position corresponding to the two voltage states of the cell.

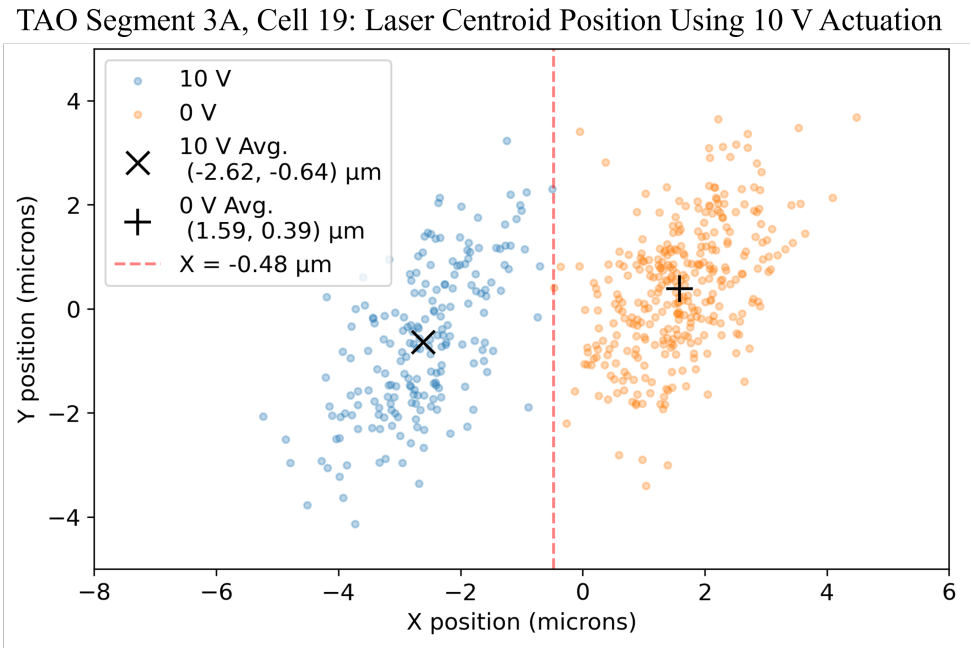

Figure 13. Laser centroid position when using discrete 10 V actuation of cell 19 of TAO Segment 3A at an ∼1 s cycle. The mean laser deflection distance between the 0 V and 10 V states was 4.33 μm.

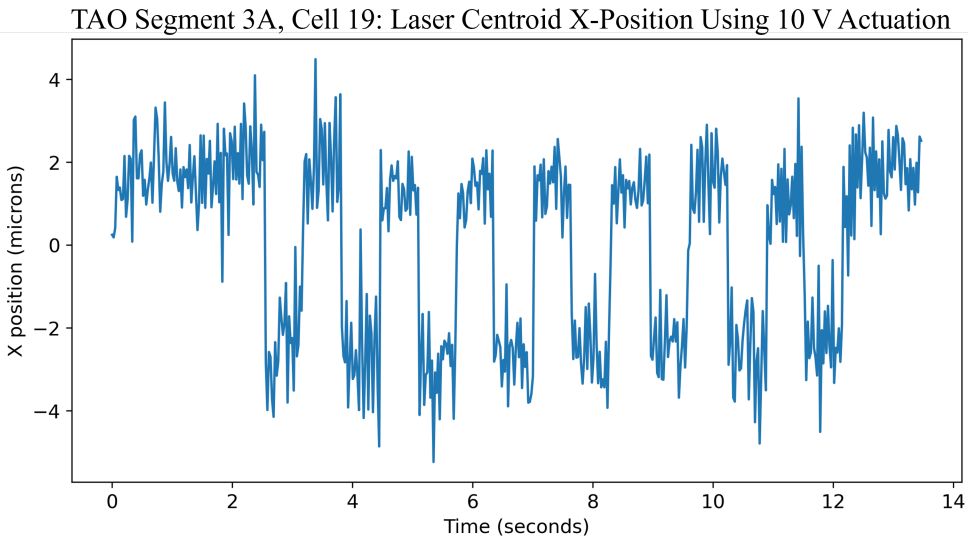

Figure 14. Laser centroid x position as a function of time when using discrete 10 V actuation of cell 19 of TAO Segment 3A at a period of ∼ 1 s. The peaks in x position correspond to the 0 V state of the cell and the valleys correspond to the 10 V state. The portion of data up to ∼2 s mark was the idle laser position before the actuation began.

The next test measured laser deflection off of cells 9–24 of Segment 3A driven simultaneously by discrete actuation using a 10 second delay between voltage states. The delay was increased when driving multiple cells simultaneously as a conservative effort to let all cells reach maximum actuation during the 10 V state and

deactuate during the 0 V state. Figure 15 shows the laser centroid position on the camera for each frame captured during the test. During the 10 V state, the laser deflected to one of several small clusters at $x < 0$ μm based on the cell it reflected from. During the 0 V state the laser converged near the (0, 0) position hence the large density of points seen in the plot.

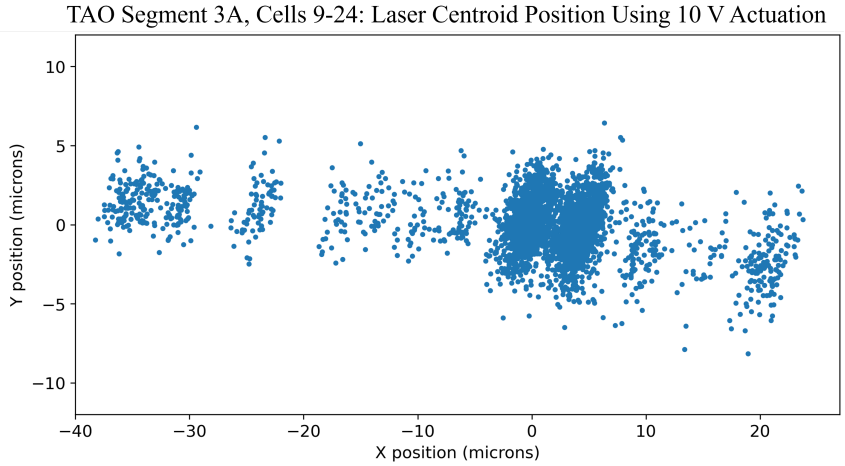

Figure 15. Laser centroid position when using discrete 10 V actuation of cells 9–24 of TAO Segment 3A simultaneously using an ∼10 s cycle. The large density of centroid points near the (0, 0) position represent the convergence of the laser position during the 0 V state of the cells.

The centroid x position was then extracted again and plotted over time in Figure 16(a). The magnitude of deflection increased due to multiple cells actuating simultaneously. The 20μm and the 0 μm x positions both correspond to the 0 V state in 16(a). The cycles of the centroid x position were then phase-shifted onto a single period as a periodogram in Figure 16(b). From this overlay of positional data, the TAO segment shows a repeatable deflection of the laser. The measured period from forming the periodogram was 14.3 seconds, slightly greater than the programmed period. This difference is attributed to a build up of software execution time over multiple cycles.

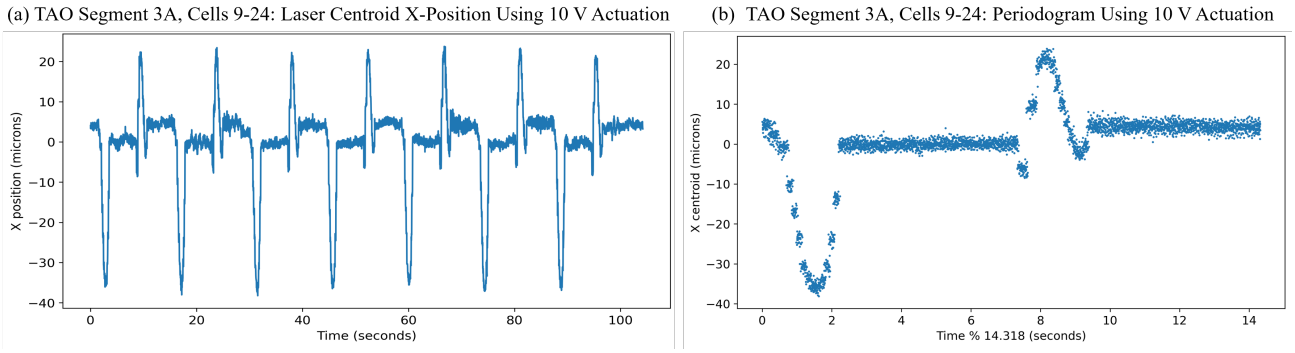

Figure 16. (a) Laser centroid x position as a function of time when using discrete 10 V actuation of cells 9–24 of TAO Segment 3A simultaneously using an ∼ 10 s cycle. (b) Periodogram of x centroid position calculated from (a). The measured period was 14.3 seconds.

The motion controllers were then swapped for a function generator to drive all cells at 100 Hz. The camera framerate was set to 644 fps, and the laser position was remeasured. Figure 17 shows the x centroid position over time. While the position does alternate between the 10 V state valley and 0 V state peak, the deflection is less repeatable than that measured during the discrete control tests. The repeatability of measuring high frequency deflections was limited in part by vibrations present in the setup used. Though the PZT response time in adaptive optics have been shown to reach resonances of > 100 kHz,[33] the current TAO devices may be

limited by their fundamental mechanical resonant frequency of the sample and its mount. Another possibility is that the inductive impedance from the cables used to drive the mirror was comparable to the piezoelectric itself, which lagged the actuation response of cells. A final possibility may be that the LRC time constant of the measurement system due to the cells having non-negligible capacitance. This can result in the voltage not building up quickly enough over the generated period which can result in slowed actuation and a distorted signal.

The average deflection between states was ~ 18 μm over a 1 second duration. The larger deflection distance observed using the 100 Hz signal over the discrete actuation is due to the larger number of cells being actuated. The figure changes of multiple cells sum together to form a larger net figure change on the segment and thus a larger deflection in the laser.

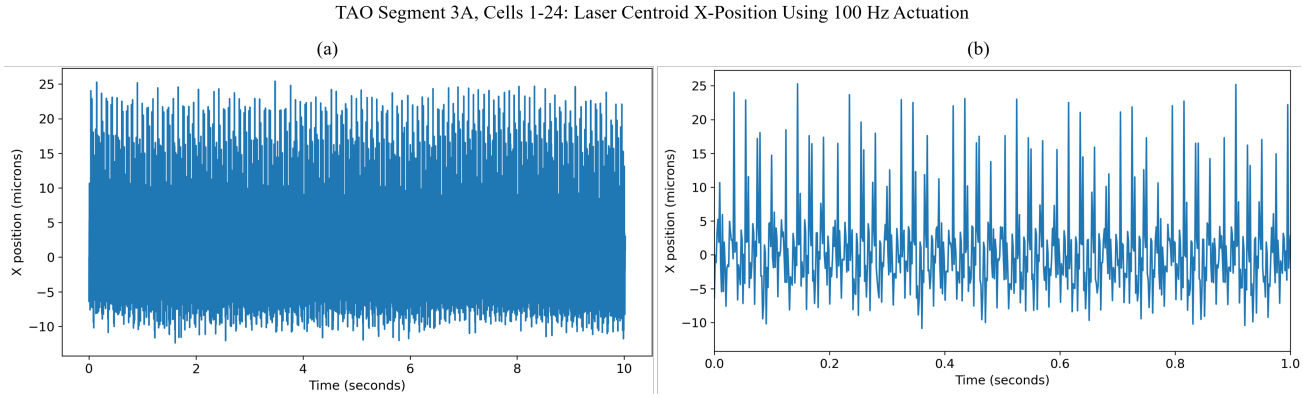

Figure 17. Laser centroid x position when using driving all cells of TAO Segment 3A at 100 Hz over a duration of (a) 10 seconds and (b) 1 second. Both figures were constructed from the same displacement test.

5. CONCLUSIONS AND FUTURE WORK

Two thin adaptive optic (TAO) segments with PZT actuator cells were successfully fabricated and interferometrically measured. Segment 2A had a surface area of 20 mm $\times$ 115 mm and included 20 cells, each of size 10 mm $\times$ 5 mm. Segment 3A had a surface area of 20 mm $\times$ 80 mm and included 24 cells, each of size 10 mm $\times$ 2.5 mm. Both segments were $\sim$ 0.5 mm thick and included a 2.8 μm thick layer of PZT as the piezoelectric material. The segments are capable of inducing localized figure changes through the application of low DC voltages to their cells meant to correct for mirror distortion as well as perform wavefront shaping in X-ray beamlines.

Fizeau interferometry was used to measure the optical surface heights of the segments and their cell responses. Segment 2A had an initial figure RMS of 6.35 μm and PV of 25.87 μm. Segment 3A had an initial figure RMS of 1.92 μm and PV of 7.58 μm. These PVs corresponded to measured radii of curvature of 57.99 m and 86.70 m for Segments 2A and 3A, respectively. Additionally, the interferometric repeatability of both segments was also measured. Segment 2A had an RMS repeatability of 0.58 nm and PVr repeatability of 2.35 nm. Segment 3A had an RMS repeatability of 0.57 nm and PVr repeatability of 6.38 nm. The repeatability was limited by the current method of taping TAOs to perfboards to allow for wire bonding of cells to control electronics.

The control electronics included a set of Galil RIO-47142 programmable logic controllers, each with 8 analog inputs/outputs operating on a range of $\pm$10 V. The simplicity of using off-the-shelf components lent to their versatility for controlling TAOs of varying cell count. Prior to measurement of cell responses, both mirrors were poled at 10 V for approximately 30 min to increase piezoelectric strain in the cells. While 10 V actuation of the TAO segments allowed for measurement of significant figure change from the cells, the maximum driving voltage of the segments is $\sim$35 V. Operating cells over the largest voltage range possible allows for the largest dynamic range of figure change, increasing their wavefront shaping capabilities. Thus, simple voltage amplifier boards are currently being prototyped to be used in conjunction with the motion controllers to increase their voltage output range. Additionally, the limitations of the control electronics resulted in incomplete poling of the PZT films. While actuation was observable, this led to non-linearities in the observed deflection and slight creep

response under prolonged actuation. Both effects can be improved through hot poling the segments, which will result in more stable film strain.

Influence functions (IFs) of both segments were measured at 10 V to observe cell response and dynamic range of figure change. Segment 2A realized 100% cell yield after measuring all 24 IFs. For Segment 3A, however, 18 out of 24 IFs were measured due to disconnects in the micro-welds made between Segment 3A and the perfboard and is not attributed to the performance of the piezoelectric cells themselves. On average, the IFs of Segment 2A and 3A induced figure PVs of 183 nm and 63 nm, respectively.

Additional tests of cell response were conducted on Segment 3A. Cell actuation linearity as a function of cell voltage was measured and exhibited a small deviation from a linear response when fit with a quadratic model. The quadratic cell response is likely due in large part to a ferroelectric hysteresis as a result of incomplete poling of the piezoelectric. The effect of applying large fields opposing the polarization direction was assessed by making measurements of a cell alternating between the -10 V, 0 V, and 10 V states. The difference between the -10 V and 10 V states showed a PV that was $\sim 22\%$ of the original IF PV, as expected due to degradation of the remanent polarization associated with applying large bipolar fields to the part without completing proper poling. This demonstrates the limit of bipolar field application in thin-film piezoelectric devices, for which modest voltages induce large electric fields. However, a small positive bias can be applied to cells for inducing negative slope changes. The cell creep response was also measured to determine actuation stability over prolonged use. The response of a single cell at 10 V was repeatedly measured for 30 min. The difference between the cell response at the beginning and end of the test showed a PV of 0.95 nm, or 1.5% the total figure change PV of the cell and is consistent with the level of metrology error in the setup. This demonstrates good stability in actuation for long duration use despite partial poling of the PZT.

Segment 3A was also used to successfully demonstrate the repeatable deflection of a laser as captured by a camera. When using 10 V discrete actuation of a single cell using 1 s cycle, the laser deflected an average distance of 4.33 μm. The same 10 V actuation was used on cells 9–24 with a programmed delay of 10 s between voltage states. A periodogram was constructed from the laser centroid lateral position and showed a repeatable cycle with a period of 14.3 seconds. This measured period was larger than the set 10 s period as a result of the buildup of software execution time over consecutive cycles. Finally, a 100 Hz signal was used to actuate all cells. The laser experienced a ~ 18 μm deflection over a 1 second duration, albeit in a less repeatable cycle due to the presence of vibrations in the setup used, and the possible limitations of the first resonance frequency of the mirror and the impedance of the cables used.

Future work for this technology development program includes improvements to TAO design and efforts to characterize their figure correction and wavefront shaping capabilities. As noted, the measured surface error PVs for the TAOs presented in this work are too large for their cells to realize absolute figure correction or wavefront shape. Thus, future versions of TAO devices will incorporate a stress compensating layer after the high temperature annealing of the PZT. The deposition parameters for the stress compensating layer can be calculated through the use of interferometry to calibrate the PV induced on a substrate when a uniform film (typically SiO_2) of known thickness is deposited on one side. Current work is constructing the methodology for depositing SiO_2 films to demonstrate stress compensation on flat, 0.5 mm thick silicon wafers. Additional fabrication changes include more robust TAO wire bonding and mounting. The current method of micro-welding makes general handling of TAOs difficult given their fragile bonds. This affects cell characterization and mirror performance given the reduced cell yield of Segment 3A. One possibility of future wire bonding would be to pattern cell traces that connect to a set of flexible anisotropic conductive film (ACF) cables. Thin-film PZT adjustable X-ray optics for use in astronomy have previously been fabricated to bond mirror segments with 288 cells.[17]

The full set of measured IFs of Segment 2A can be used to predict the relative wavefront shaping capabilities of the device. More specifically, given a target mirror wavefront shape and assuming an ideally flat initial figure, the optimal cell voltages can be calculated to induce a figure change to produce the wavefront. As discussed, one method of simulating the wavefront correction involves a matrix inversion of the IFs and a linear least-squares approach that predicts the voltages needed to scale each IF to produce the wavefront. However, this method assumes that the IFs scale linearly with voltages and co-add with other IFs linearly as well. This is worth noting since as discussed in Section 3.2, the cell response of Segment 3A was found to be closer to quadratic. Though the

observed non-linearity can be corrected for with hot poling, an alternative approach toward wavefront shaping as part of this technology development program is to use machine learning to fully characterize the TAO cell response to account for hysteresis and non-linearities. Previous work on an adaptive bimorph optic used a neural network to measure future mirror figure based on the timed history of the figure. These parameters were then used in a cost regulation algorithm to transform the mirror to a desired shape at surface error within 2 nm.[34]

ACKNOWLEDGMENTS

This work was supported by NASA awards 80NSSC24K0326 and 80NSSC22K1931. Antoine Islegen-Wojdyla and Xiaoya Chong are supported by an Early Career Award in the X-Ray Instrumentation Program, in the Science User Facility Division of the Office of Basic Energy Sciences of the U.S. Department of Energy, under Contract No. DE-AC02-05CH11231. The Advanced Light Source is supported by the Director, Office of Science, Office of Basic Energy Sciences, of the U.S. Department of Energy under Contract No. DE-AC02-05CH11231. K. Buffo acknowledges the support of the NASA FINESST grant (80NSSC23K1483) and funding from the Iowa Space Grant Consortium Graduate Student Fellowship. The authors would like to thank Phathakone Sanethavong from Lawrence Berkeley National Laboratory for his help with the wire bonding of the devices. The authors would also like to thank Samuel Hisel from University of Iowa for his help with fabricating mirror connection cables.

REFERENCES

[1] Huang, L., Bertram, L., Ma, L., Goff, N., Crane, S. W., Odate, A., Northey, T., Carrascosa, A. M., Simmermacher, M., Muvva, S. B., Geiser, J. D., Lueckheide, M. J., Phelps, Z., Liang, M., Cheng, X., Forbes, R., Robinson, J. S., Hayes, M. J., Allum, F., Green, A. E., Lopata, K., Rudenko, A., Wolf, T. J. A., Centurion, M., Rolles, D., Minitti, M. P., Kirrander, A., and Weber, P. M., "The ring-closing reaction of cyclopentadiene probed with ultrafast x-ray scattering," *The Journal of Physical Chemistry A* **128**(25), 4992–4998 (2024). PMID: 38709555.

[2] Cao, Y., Mazzone, D. G., Meyers, D., Hill, J. P., Liu, X., Wall, S., and Dean, M. P. M., "Ultrafast dynamics of spin and orbital correlations in quantum materials: an energy- and momentum-resolved perspective," *Philosophical Transactions of the Royal Society A: Mathematical, Physical and Engineering Sciences* **377**(2145), 20170480 (2019).

[3] Holler, M., Diaz, A., Guizar-Sicairos, M., Karvinen, P., Färm, E., Härkönen, E., Ritala, M., Menzel, A., Raabe, J., and Bunk, O., "X-ray ptychographic computed tomography at 16 nm isotropic 3d resolution," *Scientific Reports* **4**(1), 3857 (2014).

[4] Cocco, D. and Spiga, D., "Wavefront preserving optics for diffraction-limited storage rings and free-electron lasers," in [*X-Ray Lasers and Coherent X-Ray Sources: Development and Applications XIII*], Klisnick, A. and Menoni, C. S., eds., **11111**, 111110G, International Society for Optics and Photonics, SPIE (2019).

[5] Mills, D., Padmore, H., and Lessner, E., "X-ray optics for BES light source facilities," tech. rep., Brookhaven National Lab. (BNL), Upton, NY (United States) (03 2013).

[6] Nistea, I.-T., Alcock, S. G., Foster, A., Badami, V., Signorato, R., and Fusco, M., "Picometre-level surface control of a closed-loop, adaptive X-ray mirror with integrated real-time interferometric feedback," *Journal of Synchrotron Radiation* **32**, 133–144 (Jan 2025).

[7] Matsuyama, S., Nakamori, H., Goto, T., Kimura, T., Khakurel, K. P., Kohmura, Y., Sano, Y., Yabashi, M., Ishikawa, T., Nishino, Y., and Yamauchi, K., "Nearly diffraction-limited x-ray focusing with variable-numerical-aperture focusing optical system based on four deformable mirrors," *Scientific Reports* **6**(1), 24801 (2016).

[8] Walker, J., Liu, T., Tendulkar, M., Burrows, D., DeRoo, C., Allured, R., Hertz, E., Cotroneo, V., Reid, P., Schwartz, E., Jackson, T., and Trolier-McKinstry, S., "Design and fabrication of prototype piezoelectric adjustable x-ray mirrors," *Optics Express* **26**, 27757 (10 2018).

[9] DeRoo, C. T., Allured, R., Cotroneo, V., Hertz, E. N., Marquez, V., Reid, P. B., Sr., E. D. S., Vikhlinin, A. A., Trolier-McKinstry, S., Walker, J., Jackson, T. N., Liu, T., and Tendulkar, M., "Deterministic figure correction of piezoelectrically adjustable slumped glass optics," *Journal of Astronomical Telescopes, Instruments, and Systems* **4**(1), 019004 (2018).

[10] Polcawich, R. G. and Trolier-McKinstry, S., "Piezoelectric and dielectric reliability of lead zirconate titanate thin films," *Journal of Materials Research* **15**(11), 2505–2513 (2000).

[11] Bassiri-Gharb, N., Fujii, I., Hong, E., Trolier-McKinstry, S., Taylor, D., and Damjanovic, D., "Domain wall contributions to the properties of piezoelectric thin films," *Journal of Electroceramics* **19**, 49–67 (01 2007).

[12] Chima-Okereke, C., Reece, M. J., Bushby, A. J., Whatmore, R. W., and Zhang, Q., "Nanoindentation of multilayer PZT/Pt/SiO_2 thin film systems on silicon wafers for MEMS applications," *MRS Online Proceedings Library* **841**(1), R12.3 (2005).

[13] Guarnieri, V., Biazi, L., Marchiori, R., and Lago, A., "Platinum metallization for mems application. focus on coating adhesion for biomedical applications," *Biomatter* **4**, e28822 (2014).

[14] Doi, T., Noguchi, T., Fuji, J., Soyama, N., and Sakurai, H., "The orientation and grain texture effect on life time reliability of sol-gel derived pbzr0.52ti0.48o3 films," *Japanese Journal of Applied Physics* **51**, 09LA15 (sep 2012).

[15] Tipsawat, P., *Released Piezoelectric Thin Films For Piezoelectric Micromachined Ultrasound Transducers (PMUT)*, ph.d. dissertation, Pennsylvania State University, State College, USA (2024).

[16] Garino, T. J. and Harrington, M., "Residual stress in pzt thin films and its effect on ferroelectric properties," *MRS Online Proceedings Library* **243**(1), 341–347 (1991).

[17] Buffo, K., DeRoo, C., Reid, P., Kradinov, V., Marquez, V., Trolier-McKinstry, S., Bishop, N., Jackson, T. N., Tran, Q., Liang, H., and Tendulkar, M., "Adjustable X-ray optics: thin-film actuator measurement and figure correction performance," *Journal of Astronomical Telescopes, Instruments, and Systems* **10**(3), 039003 (2024).

[18] 4D Technology Corporation, *AccuFiz Fizeau Interferometer Fact Sheet* (2017). `https://www.4dtechnology.com/wp-content/uploads/Data_Sheets/AccuFiz_Fact_Sheet.pdf`.

[19] Brock, N., Hayes, J., Kimbrough, B., Millerd, J., North-Morris, M., Novak, M., and Wyant, J. C., "Dynamic interferometry," in [*Novel Optical Systems Design and Optimization VIII*], Sasian, J. M., Koshel, R. J., and Juergens, R. C., eds., **5875**, 58750F, International Society for Optics and Photonics, SPIE (2005).

[20] Bishop, N. L., Kradinov, V., Reid, P. B., Jackson, T. N., DeRoo, C. T., and Trolier-McKinstry, S., "Stress-balancing in piezoelectric adjustable x-ray optics," *Journal of Astronomical Telescopes, Instruments, and Systems* **8**(2), 029004 (2022).

[21] 4D Technology Corporation, *AccuFiz Compact Fizeau Interferometer Specifications* (2023). `https://www.4dtechnology.com/wp-content/uploads/Data_Sheets/AccuFiz_Data_Sheet.pdf`.

[22] Buffo, K., DeRoo, C., Reid, P., Kradinov, V., Marquez, V., Trolier-McKinstry, S., Bishop, N., Jackson, T. N., Tran, Q., Liang, H., Liu, T., and Tendulkar, M., "Thin-film PZT actuator performance in adjustable x-ray optic segments," in [*Optics for EUV, X-Ray, and Gamma-Ray Astronomy XI*], O'Dell, S. L., Gaskin, J. A., Pareschi, G., and Spiga, D., eds., **12679**, 1267915, International Society for Optics and Photonics, SPIE (2023).

[23] Buffo, K., "axroGalil Repository," (2023). `https://github.com/kbuffo/axroGalil`.

[24] Trolier-McKinstry, S., [*Crystal Chemistry of Piezoelectric Materials*], 39–56, Springer US, Boston, MA (2008).

[25] Liu, T., Wallace, M., Trolier-McKinstry, S., and Jackson, T. N., "High-temperature crystallized thin-film pzt on thin polyimide substrates," *Journal of Applied Physics* **122**, 164103 (10 2017).

[26] Wang, W., Chen, Z., Zhou, Z., Li, Y., and Liang, R., "Enhancing electromechanical properties of pzt-based piezoelectric ceramics by high-temperature poling for high-power applications," *ACS Applied Materials & Interfaces* **15**(12), 15636–15645 (2023). PMID: 36929757.

[27] Love, A. E. H. and Darwin, G. H., "Xvi. the small free vibrations and deformation of a thin elastic shell," *Philosophical Transactions of the Royal Society of London. (A.)* **179**, 491–546 (1888).

[28] Xia, R., Fan, H., and Woo, C., "Dynamic process of domain switching in ferroelectric films," *Journal of Applied Physics* **94**, 3384 (09 2003).

[29] ZWO Optical, "Asi6200 pro series." `https://www.zwoastro.com/product/asi6200/` (n.d.). Accessed June 23, 2025.

[30] Signorato, R., Hignette, O., and Goulon, J., "Multi-segmented piezoelectric mirrors as active/adaptive optics components," *Journal of Synchrotron Radiation* **5**, 797–800 (May 1998).

[31] Alcock, S. G., Nistea, I.-T., Badami, V. G., Signorato, R., and Sawhney, K., "High-speed adaptive optics using bimorph deformable x-ray mirrors," *Review of Scientific Instruments* **90**, 021712 (02 2019).

[32] Yan, S., Jiang, H., Jiang, Z., Liang, D., Xie, J., Zhu, H., Shu, G., Ben, N., and Li, A., "X-ray speckle reduction using a high-speed piezoelectric deformable mirror system," *High Power Laser Science and Engineering* **13**, e22 (2025).

[33] Briles, T. C., Yost, D. C., Cingöz, A., Ye, J., and Schibli, T. R., "Simple piezoelectric-actuated mirror with 180 khz servo bandwidth," *Optics Express* **18**, 9739 (Apr. 2010).

[34] Gunjala, G., Wojdyla, A., Goldberg, K. A., Qiao, Z., Shi, X., Assoufid, L., and Waller, L., "Data-driven modeling and control of an x-ray bimorph adaptive mirror," *Journal of Synchrotron Radiation* **30**(Pt 1), 57–64 (2023).